NJC

PAPER

View Article Online
View Journal | View Issue

Cite this: *New J. Chem.*, 2019, **43**, 6032

A quantitative description of photoluminescence efficiency of a carbazole-based thermally activated delayed fluorescence emitter†

Songyan Feng, Xugeng Guo * and Jinglai Zhang *

Received 8th January 2019,
Accepted 14th March 2019

DOI: 10.1039/c9nj00101h

rsc.li/njc

A reliable quantitative description of photoluminescence efficiency is crucial for designing and developing new-type thermally activated delayed fluorescence (TADF) emitters. In this contribution, we computed the conversion and decay rates of a novel TADF-active molecule, 2-(9*H*-carbazol-9-yl)-thianthrene-5,5,10,10-tetraoxide (CZ-TTR), involving the lowest singlet excited S_1 state and triplet excited T_1 state. The efficiency of total fluorescence containing prompt fluorescence and delayed fluorescence was obtained correspondingly. The present results reveal that the rate of reverse intersystem crossing from T_1 to S_1 is calculated to be slightly larger than the radiative and non-radiative decay rates of the S_1 state at 300 K temperature, thus resulting in an occurrence of delayed fluorescence. Additionally, the total fluorescence efficiency is estimated to be 54.5%, which agrees very well with the photoluminescence quantum yield of 56.7% observed experimentally. It is also found that the dominant charge transfer characteristics in the S_1 and T_1 states produce a small energy difference between the two states, and consequently an efficient reverse intersystem crossing process and a high fluorescence efficiency.

1 Introduction

In recent years, the photoluminescence properties of thermally activated delayed fluorescence (TADF) emitters have received intense scientific interest, owing to their promising applications as organic light-emitting diodes (OLEDs) for display and illumination.[1–6] In OLED devices, TADF emitters can produce light by harvesting both singlet and triplet excitons without employing any noble metals, which provides an efficient pathway to achieve an internal quantum efficiency (IQE) of 100%, thus breaking the limitation of 25% IQE in conventional fluorescent OLEDs as a consequence of spin statistics. For this reason, a large number of red, green and even blue TADF-based OLED materials have been developed.[7–40]

It has been generally accepted that an efficient TADF emitter needs a small singlet–triplet energy difference (ΔE_{ST}) to achieve an efficient reverse intersystem crossing (RISC) from the lowest excited triplet T_1 state to the lowest excited singlet S_1 state, which requires an effective separation of the highest-occupied molecular orbital (HOMO) and the lowest-unoccupied molecular orbital (LUMO).[41] Meanwhile, a spatial overlap between HOMO and LUMO is also very important to obtain a high photoluminescence quantum yield (PLQY). Based on these criteria, the TADF emitters are commonly designed by combining the electron donor (D) and electron acceptor (A) fragments within one molecule. By using the carbazole (CZ) group as the D unit and the thianthrene tetraoxide (TTR) group as the A moiety, Wang *et al.* recently designed and synthesized a new D–A-type emitter, 2-(9*H*-carbazol-9-yl)-thianthrene-5,5,10,10-tetraoxide (**CZ-TTR**, see Fig. 1).[42] It was found that the ΔE_{ST} value and PLQY value were measured to be 0.10 eV and 56.7% in a **CZ-TTR** doped mCP film, respectively, giving rise to a maximum external quantum efficiency (EQE) of 14.4%.[42] Moreover, the fluorescence peak in the same film was measured at 487 nm, due to which it has been considered as an efficient blue TADF emitter.[42]

In addition to a wealth of experimental literature presenting TADF, theoretical studies mainly concern the geometric structures of ground S_0 states and excited states, singlet–triplet energy difference, and ultraviolet absorption and fluorescence emission spectra by employing density functional theory (DFT) and time-dependent density functional theory (TD-DFT) computational approaches.[43–45] However, quantitative predictions on fluorescence efficiencies of the TADF molecules are still scarce.[46–48] In the present work, we herein performed a comprehensive computational

Henan Provincial Engineering Research Center of Green Anticorrosion Technology for Magnesium Alloy, College of Chemistry and Chemical Engineering, Henan University, Kaifeng 475004, P. R. China. E-mail: xgguo@henu.edu.cn, zhangjinglai@henu.edu.cn

† Electronic supplementary information (ESI) available: Geometry comparisons between S_0 and S_1 calculated using different density functionals. Reorganization energy of each normal vibration mode calculated using different density functionals. Reorganization energies from bond length, bond angle, and dihedral angle in the gas phase. Excited-state decay rate constants obtained by the M06-HF/B3LYP hybrid calculations at different temperatures. See DOI: 10.1039/c9nj00101h

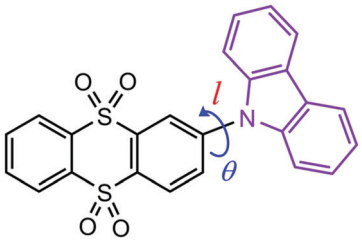

Fig. 1 Chemical structure of **CZ-TTR**. θ and l represent the dihedral angle and bond length between the donor and acceptor moieties, respectively.

study on the **CZ-TTR** molecule, since it has numerous photophysical and spectroscopic data in experiments. The excited-state decay and conversion processes were quantitatively computed by using the thermal vibration correlation function (TVCF) rate formalism developed by Shuai group,[49] including the radiative decay (k_r^S and k_r^T) and non-radiative decay (k_{nr}^S and k_{nr}^T) from S_1/T_1 to S_0, as well as the intersystem crossing from S_1 to T_1 (k_{ISC}) and reverse intersystem crossing from T_1 to S_1 (k_{RISC}). On the other hand, the prompt fluorescence efficiency (Φ_{PF}), delayed fluorescence efficiency (Φ_{DF}), and the total fluorescence efficiency (Φ_F) were obtained correspondingly. It is expected that the present computational results can serve as a theoretical guide for designing and developing new-type highly-efficient OLED materials based on TADF emitters.

2 Theoretical method and computational details

2.1 Theoretical method

For a TADF molecule, the total fluorescence efficiency (Φ_F) is the sum of the prompt fluorescence efficiency (Φ_{PF}) and delayed fluorescence efficiency (Φ_{DF}), which can be written as:[50]

$$\Phi_F = \Phi_{PF} + \Phi_{DF} \quad (1)$$

$$\Phi_{PF} = \frac{k_r^S}{k_r^S + k_{nr}^S + k_{ISC}} \quad (2)$$

$$\Phi_{DF} = \frac{\Phi_{ISC}\Phi_{RISC}}{1 - \Phi_{ISC}\Phi_{RISC}}\Phi_{PF} \quad (3)$$

where k_r^S and k_{nr}^S denote the radiative and non-radiative decay rates of the S_1 state, respectively, and Φ_{ISC} and Φ_{RISC} represent the intersystem crossing efficiency and reverse intersystem crossing efficiency, respectively, both of which can be expressed by the following equations

$$\Phi_{ISC} = \frac{k_{ISC}}{k_r^S + k_{nr}^S + k_{ISC}} \quad (4)$$

$$\Phi_{RISC} = \frac{k_{RISC}}{k_r^T + k_{nr}^T + k_{RISC}} \quad (5)$$

where k_r^T and k_{nr}^T are the radiative and non-radiative decay rates of the T_1 state, respectively. It should be noted that the k_r^T can be neglected for organic molecules since it has a negligible effect on the Φ_{RISC} result as found in a previous study.[47] k_{ISC} and k_{RISC} are the intersystem crossing rate from S_1 to T_1 and reverse intersystem crossing rate from T_1 to S_1, respectively.

In the present calculations, the radiative decay rate can be estimated as follows

$$k_r = \int \sigma_{em}(\omega, T)\mathrm{d}\omega \quad (6)$$

where $\sigma_{em}(\omega, T) = \frac{4\omega^3}{3\hbar c^3}\sum_{u,v} P_{iv}|\langle \Theta_{fu}|u_{fi}|\Theta_{iv}\rangle|^2 \delta(\omega_{iv,fu} - \omega)$. $u_{fi} = \langle \Phi_f|\hat{\mu}|\Phi\rangle_i$ denotes the electronic transition dipole moment between two electronic states $|\Phi_f\rangle$ and $|\Phi_i\rangle$; P_{iv}, the initial state Boltzmann distribution function; Θ, the nuclear vibrational wave function, and u and v, vibrational quantum numbers.

The non-radiative decay rate can be evaluated in the framework of Fermi golden rule and first-order perturbation theory:

$$k_{nr} = \frac{2\pi}{\hbar}\sum_{v,u} P_{iv}\left|H_{fu,iv}{}' + \sum_{n,\mu}\frac{H_{fu,n\mu}{}' H_{n\mu,iv}{}'}{E_{iv} - E_{n\mu}}\right|^2 \delta(E_{iv} - E_{fu}) \quad (7)$$

where H' represents the interaction between two different Born–Oppenheimer states, which is composed of two contributions as follows:

$$\hat{H}'\Psi_{iv} = \hat{H}^{BO}\Phi_i(\mathbf{r};\mathbf{Q})\Theta_v(\mathbf{Q}) + \hat{H}^{SO}\Phi_i(\mathbf{r};\mathbf{Q})\Theta_v(\mathbf{Q}) \quad (8)$$

Here $\hat{H}^{BO}$ is the non-adiabatic coupling, and $\hat{H}^{SO}$ is the spin–orbit coupling.

The intersystem crossing rate from initial singlet/triplet to triplet/singlet states can be recast on the basis of the second-order perturbation theory as

$$k_{f\leftarrow i}^{ISC} = k_{f\leftarrow i}^{(0)} + k_{f\leftarrow i}^{(1)} + k_{f\leftarrow i}^{(2)} \quad (9)$$

where

$$k_{f\leftarrow i}^{(0)} \equiv \frac{1}{\hbar^2}|H_{fi}^{SO}|^2\int_{-\infty}^{\infty}\mathrm{d}t e^{i\omega_{if}t}\rho_{fi}^{(0)}(t) \quad (10)$$

$$k_{f\leftarrow i}^{(1)} \equiv \mathrm{Re}\left[\frac{2}{\hbar^2}\sum_k H_{fi}^{SO}T_{if,k}\int_{-\infty}^{\infty}\mathrm{d}t e^{i\omega_{if}t}\rho_{fi,k}^{(1)}(t)\right] \quad (11)$$

$$k_{f\leftarrow i}^{(2)} \equiv \frac{1}{\hbar^2}\sum_{k,l} T_{if,k}T_{if,l}\int_{-\infty}^{\infty}\mathrm{d}t e^{i\omega_{if}t}\rho_{fi,kl}^{(2)}(t) \quad (12)$$

Here $\rho_{fi}^{(0)}(t) \equiv Z_i^{-1}\mathrm{Tr}[e^{-i\tau_f\hat{H}_f}e^{-i\tau_i\hat{H}_i}]$, $\rho_{fi,k}^{(1)}(t) \equiv Z_i^{-1}\mathrm{Tr}[\hat{P}_{fk}e^{-i\tau_f\hat{H}_f}e^{-i\tau_i\hat{H}_i}]$, $\rho_{fi,kl}^{(2)}(t) \equiv Z_i^{-1}\mathrm{Tr}[\hat{P}_{fk}e^{-i\tau_f\hat{H}_f}\hat{P}_{fl}e^{-i\tau_i\hat{H}_i}]$, $T_{if,k(l)}$ is the mixed spin–orbit and non-radiative coupling between two electronic states for the $k(l)$th normal mode. Owing to the spin symmetry requirement, for the first-order contribution $k_{f\leftarrow i}^{(0)}$, the $\hat{H}^{BO}$ term in eqn (8) does not make any contribution between the singlet and triplet states. Accordingly, the simplest and most commonly used intersystem crossing rate formalism can be expressed as

$$k_{ISC} = \frac{1}{\hbar^2}\langle \Phi_f|\hat{H}^{SO}|\Phi_i\rangle\int_{-\infty}^{\infty}\mathrm{d}t\left[e^{i\omega_{if}t}Z_i^{-1}\rho_{ISC}(t,T)\right] \quad (13)$$

Both the methodology and application of these rate equations can be seen in the studies by the Peng and Shuai groups.[49,51,52]

2.2 Computational details

Structural optimization and frequency computation of **CZ-TTR** in the gas phase were carried out for the S_0 state by DFT, and for the S_1 and T_1 states by TD-DFT. Five exchange–correlation functionals, that is, B3LYP (20% HF), PBE0 (25% HF), BMK (42% HF), M06-2X (54% HF), and M06-HF (100% HF), as well as one range-separated hybrid functional, ωB97X, were employed along with the 6-31G* basis set. All the calculations were performed using the Gaussian 09 program.[53]

According to the electronic properties obtained, the rates of radiative, non-radiative, intersystem crossing, and reverse intersystem crossing were estimated by using the TVCF theory, as performed in the molecular materials property prediction package (MOMAP).[49,52,54,55] The transition electric field was calculated by TD-DFT with the Gaussian 09 package. The spin–orbit coupling (SOC) calculations were implemented with quadratic response function methods,[56] which can be realized using the Dalton program.[57]

3 Results and discussion

3.1 Functional test

In the present study, the DFT/TD-DFT computational approaches were employed to explore the geometric and electronic properties of the title molecule. It is accepted that the properties of the D–A-type TADF-active molecules are closely related to the density functionals used in calculations.[46,58] To find a suitable functional for the present system, the molecular structures of **CZ-TTR** in the S_0, S_1 and T_1 states were optimized using different functionals. The key structural parameters and the total reorganization energies (λ_{reorg}) on the S_0 potential energy surface are summarized in Table 1. Geometrical comparisons between the S_0 and S_1 states and the reorganization energy of each normal vibration mode calculated using different functionals are plotted in Fig. S1 and S2 of the ESI.†

The structural modifications between S_1 and S_0 play a crucial role in the excited state and photoluminescence properties in that they can significantly control the optical spectrum shape and the non-radiative decay rate on the basis of the Franck–Condon principle.[59] As can be seen from Table 1, the changes of bond lengths between the D and A moieties are insusceptible to the functionals employed in calculations, with the $|\Delta l|$ value less than 0.05 Å. However, the variations of torsional angles are very sensitive to the selected functionals. For the M06-HF functional, the $|\Delta\theta|$ value is predicted to be only 2.3°, far smaller than the results calculated for five other functionals, exhibiting the smallest geometrical modification from S_1 to S_0, which is consistent with the strong fluorescence observed experimentally.[42] As a result, the λ_{reorg} value estimated by M06-HF is also known to be the smallest among those of the functionals considered here (only 0.30 eV). Accordingly, the M06-HF-optimized structures seem to be the most reasonable to evaluate the ground-state and excited-state geometries of **CZ-TTR**.

Under the M06-HF-optimized S_1 minimum, we simulated the fluorescence emission spectra of **CZ-TTR** in the gas phase at different density functional levels. The related calculated results are listed in Table 2, along with the available experimental values.[42] As shown in Table 2, the λ_{fluo} value gradually decreases with increasing HF exchange percentage. The long-range corrected functional ωB97X also dramatically underestimate the λ_{fluo} value. It is therefore evident that the value of λ_{fluo} calculated using the B3LYP functional is in best agreement with the experimental value measured in the **CZ-TTR** doped mCP film at 77 K (478 *vs.* 487 nm). In view of this, it is plausible that the hybrid approach of M06-HF for geometric optimization and frequency computation as well as B3LYP for electronic properties is suitable for the **CZ-TTR** molecule.

3.2 Singlet–triplet energy difference

It is known that $T_1 \rightarrow S_1$ RISC is an important non-radiative decay process, mainly determined by the energy difference (ΔE_{ST}) and spin–orbit coupling (SOC) between the S_1 and T_1 states. In general, the SOC constant of pure organic molecules is very weak (a few tenths of cm^{-1}) as for other organic molecules presented before,[48,58] owing to the spin-forbidden transition between the S_1 and T_1 states in the TADF emitter. For the present system, the SOC is calculated to be only 0.48 cm^{-1}. However, a small ΔE_{ST} makes the RISC process feasible. To provide a reliable prediction on the k_{RISC} rate, the ΔE_{ST} values were calculated at different density functional levels with the M06-HF-optimized geometries. The related results, along with the experimental findings, are collected in Table 2. As can be noticed from Table 2, the ΔE_{ST} value predicted by M06-HF is 0.80 eV, much larger than the experimental value measured in the mCP film at 77 K. However, B3LYP gives the most reasonable

Table 1 The bond lengths (l, in Å), dihedral angles (θ, in deg.) and reorganization energies (λ_{reorg}, in eV) for the $S_1 \rightarrow S_0$ transition obtained at different functional levels

	S_0 geometry		S_1 geometry				
Functional	θ	l	θ	l	$\lvert\Delta\theta\rvert^a$	$\lvert\Delta l\rvert^a$	λ_{reorg}
B3LYP	48.9	1.41	90.7	1.45	41.8	0.04	0.66
PBE0	48.9	1.40	91.1	1.44	42.2	0.04	0.61
BMK	48.7	1.40	89.3	1.43	40.6	0.03	0.57
M06-2X	47.4	1.40	90.8	1.43	43.4	0.03	0.42
M06-HF	51.0	1.40	53.3	1.38	2.3	0.02	0.30
ωB97X	50.9	1.41	91.9	1.43	41	0.02	0.73

[a] Changes of the dihedral angle and bond length from S_1 to S_0.

Table 2 Fluorescence wavelength (λ_{fluo}, in nm) at the S_1 minimum, emissive oscillator strength (f) and adiabatic energy difference (ΔE_{ST}, in eV) of **CZ-TTR** predicted at different density functional levels, in comparison with the experimental values

	B3LYP	PBE0	BMK	M06-2X	M06-HF	ωB97X	Exp.
HF (%)	20	25	42	54	100	—	—
λ_{fluo}	478	452	399	378	332	373	487[a]
f	0.1191	0.1293	0.1610	0.1790	0.2469	0.1827	
ΔE_{ST}	0.03	0.18	0.39	0.46	0.80	0.68	0.10[b]

[a] Fluorescence spectrum measured for the **CZ-TTR** doped mCP film at 77 K.[42] [b] Energy difference from the onsets of the fluorescence and phosphorescence spectra of **CZ-TTR** in the mCP film at 77 K.[42]

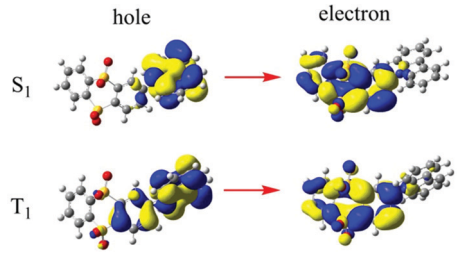

Fig. 2 Natural transition orbital (NTO) analyses for the S_1 and T_1 excited states.

Table 3 Calculated charge transfer (CT) and local excitation (LE) characteristics (in %) for the S_1 and T_1 excited states

State	CT	LE
S_1	89.9	10.1
T_1	76.9	23.1

ΔE_{ST} (0.03 eV), in comparison with the measured value of 0.10 eV.[42] This again proves that the B3LYP functional can offer a reliable prediction on the electronic properties of **CZ-TTR**. Therefore, the B3LYP-calculated singlet–triplet energy difference would be applied for the following rate calculations.

To provide a deeper understanding of the nature of the optimized excited states, natural transition orbital (NTO) analyses were also performed, which are shown in Fig. 2. For the S_1 state, the hole (in the HOMO) is mainly distributed on the CZ group, while the electron (in the LUMO) is mainly localized on the TTR moiety. This is a clear indication that the S_1 state of **CZ-TTR** exhibits the significant charge transfer (CT) characteristics. A similar trend has also been found in the T_1 state. The quantitative CT characteristics of the S_1 and T_1 states could be calculated by using the multifunctional wavefunction analyzer (Multiwfn),[60] as can be seen in Table 3. As expected, the CT components of the S_1 and T_1 states are 89.9% and 76.9%, respectively. Such a remarkable CT characteristic in both S_1 and T_1 states leads to a small overlap between HOMO and LUMO and thus a small ΔE_{ST}.

3.3 Huang–Rhys factor and reorganization energy

To determine the structure–property relationship during the $S_1 \leftrightarrow T_1$ and $S_1 \rightarrow S_0$ energy conversion processes, both the Huang–Rhys (HR) factor and reorganization energy were estimated in the present calculations. The HR factor was computed by the following equation $\mathrm{HR}_k = \frac{\omega_k D_k^2}{2}$, where ω_k is the vibration frequency and D_k is the normal coordinate displacement of mode k. Reorganization energy $\left(\lambda = \sum_k \omega_k \mathrm{HR}_k\right)$ was calculated by using the normal mode method in consideration of zero-point energy correction.

Fig. 3 shows the HR factors *versus* the normal mode frequencies of energy conversion between S_1 and T_1 in the gas phase. The large HR factors 31.6 (16.53 cm^{-1}) and 1.7 (22.23 cm^{-1}) correspond to the torsional motions (shown as insets) of the CZ group, which suggest that the free rotation of CZ provides an important channel

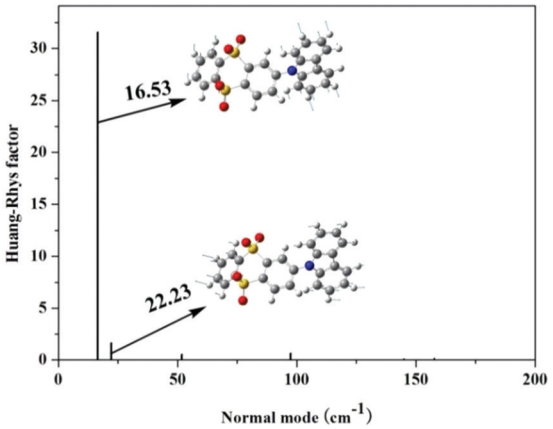

Fig. 3 Huang–Rhys factors *versus* the normal mode frequencies for energy conversion between S_1 and T_1, as well as two important vibration modes.

for the energy conversion between S_1 and T_1. For the decay process from S_1 to S_0, as shown in Fig. 4a, the representative large HR factors 3.5 (14.54 cm^{-1}), 2.9 (23.50 cm^{-1}) and 1.0 (48.90 cm^{-1}) correspond to the torsional motions of the CZ donor and TTR acceptor in low frequency regions (<200 cm^{-1}). This indicates that the rotations of D and A units play a dominant role in determining the non-radiative decay rate from S_1 to S_0. On the

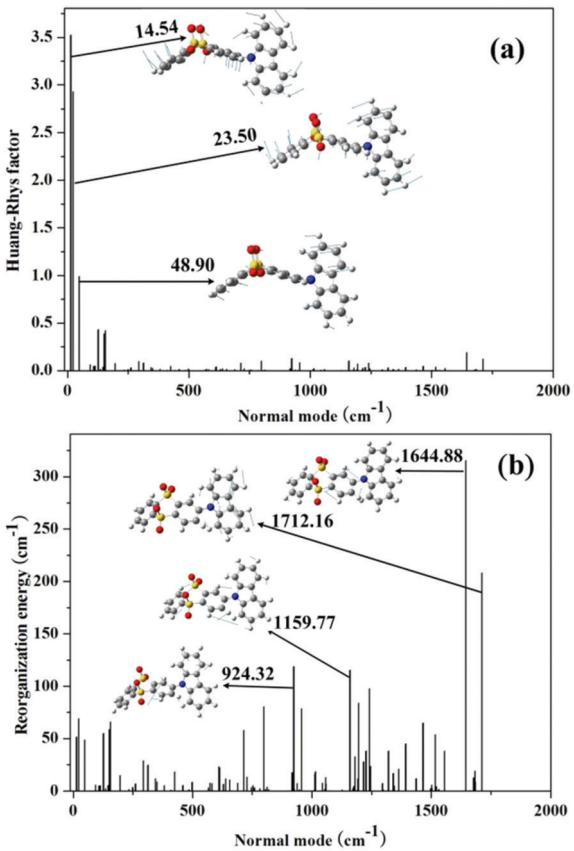

Fig. 4 Huang–Rhys factors *versus* the normal mode frequencies (a) and reorganization energy *versus* the normal mode frequencies (b) for energy conversion from S_1 to S_0, as well as the corresponding vibration modes.

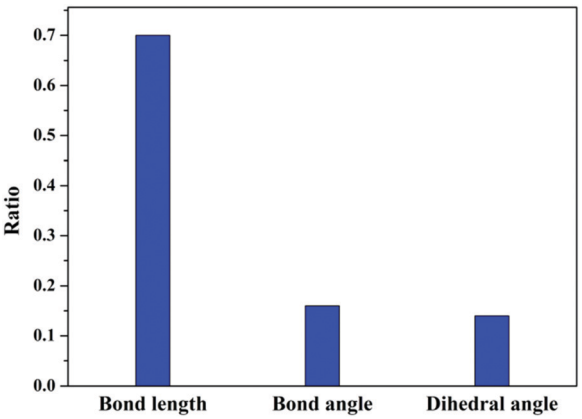

Fig. 5 Contribution ratios to the reorganization energy of **CZ-TTR** from bond lengths, bond angles, and dihedral angles.

other hand, the reorganization energies *versus* the normal mode frequencies in the gas phase are shown in Fig. 4b. The vibration modes with larger reorganization energies occur in high frequency regions, such as 924.32 cm^{-1}, 1159.77 cm^{-1}, 1644.88 cm^{-1}, and 1712.16 cm^{-1}. To better understand the relationship between the photophysical properties and the molecular structure, we have projected the reorganization energies onto the internal coordinate of the molecule. Contributions from bond lengths, bond angles, and dihedral angles are shown in Fig. 5, and the corresponding data are shown in Table S1 of the ESI.† It can be seen that the reorganization energy is mainly contributed from bond length, and its value is 210.7 meV (70.6%). It is therefore apparent that the torsional motions between the D and A units in low frequency regions and the stretching vibrations of the bonds in high frequency regions account for the non-radiative decay from S_1 to S_0.

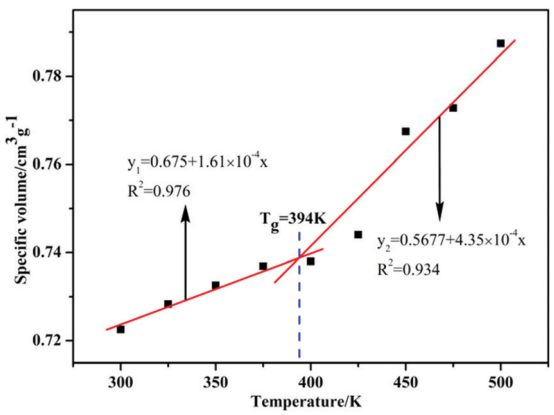

Fig. 6 The curves of specific volume-temperature for **CZ-TTR**.

3.4 Thermal property

The glass transition temperature (T_g) is an important characteristic parameter for the material, and the higher T_g indicates the greater stability of the amorphous state.[61] To evaluate the T_g of **CZ-TTR** and explore the thermostability, molecular dynamics (MD) simulations were performed by changing the specific volume at different temperatures based on the Forcite module in Materials Studio 7.0 program package.[62] The COMPASS force field[63–65] was used during each stage of the simulations. The molecular model was constructed by using 10 molecules in an amorphous cell calculation module with a size of 17.9 Å × 17.9 Å × 17.9 Å, and after optimization the model was annealed at 300–500 K. To obtain the parameters at 500 K, MD simulation was carried out by using an *NVT* ensemble for 100 ps and an *NPT* ensemble for 300 ps successively with a time step of 1.0 fs. Similarly, the MD simulation of the molecular model was performed at intervals of 25 K stepwise cooling from 500 to 300 K. The specific volume data at different temperatures were obtained and plotted. It is seen that the specific volume first rises slowly with an increase of temperature, indicating that the material is in the glassy state. When the temperature reaches a certain value, the specific volume increases drastically with increasing temperature. At this time, it is in the high elastic state. The intersection of the upper and lower fitted lines is the glass transition temperature. As shown in Fig. 6, the T_g of **CZ-TTR** is estimated to be 394 K which is in good agreement with the experimental value of 397 K (124 °C),[42] exhibiting good thermostability and thus ensuring the applications in OLED devices.

3.5 Fluorescence efficiency

The TVCF rate formula based on the first-order perturbation theory was applied to estimate the interconversion rate constants among the S_0, S_1, and T_1 states. According to the geometric/electronic properties obtained by the hybrid M06-HF/B3LYP approach, the calculated rates constants are reported in Table 4. In addition, the prompt fluorescence and delayed fluorescence efficiencies, and the total fluorescence efficiency are also incorporated in Table 4.

It can be seen from Table 4 that the k_{RISC} rate is calculated to be 9.41 × 10^5 s^{-1}, about one order of magnitude larger than the experimental value of 4.70 × 10^4 s^{-1}.[42] The k_{ISC} rate is predicted to be 1.75 × 10^6 s^{-1}, about one order of magnitude smaller than the experimental value of 1.00 × 10^7 s^{-1}.[42] Obviously, the $T_1 \rightarrow S_1$ RISC can compete with the radiative and non-radiative decay

Table 4 Calculated the radiative and non-radiative rates from S_1/T_1 to S_0, the ISC and RISC rates between S_1 and T_1 excited states and the fluorescence efficiencies, together with the available experimental data

	k_r^S	k_{nr}^S	k_r^T	k_{nr}^T	k_{ISC}	k_{RISC}	Φ_{PF}	Φ_{DF}	Φ_F
Cal.	3.47 × 10^5	1.04 × 10^5	0.87	1.13 × 10^5	1.75 × 10^6	9.41 × 10^5	15.8	38.7	54.5
Exp.[a]	4.20 × 10^6	—	—	2.19 × 10^4	1.00 × 10^7	4.70 × 10^4	29.4	27.3	56.7

[a] Experimental value from ref. 42.

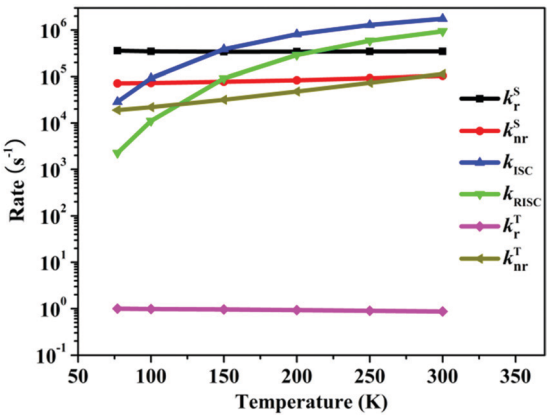

Fig. 7 Temperature dependence of the interconversion and decay rates for **CZ-TTR**.

from S_1/T_1 to S_0, in favor of the occurrence of RISC. On the basis of our calculated rate constants, the values of Φ_{PF}, Φ_{DF}, and Φ_F can be obtained. Significant prompt fluorescence (Φ_{PF} = 15.8%), delayed fluorescence (Φ_{DF} = 38.7%) and total fluorescence efficiency (Φ_F = 54.5%) are also obtained in the gas phase. All these data are in reasonable agreement with the available experimental findings measured in the **CZ-TTR** doped mCP film.[42] Moreover, the temperature dependence of interconversion rate constants was calculated, as shown in Fig. 7. The detailed data are provided in Table S2 of the ESI.† As temperature increases, the k_{ISC} and k_{RISC} rates are remarkably increased, while there are no obvious changes for other rates constants. At 300 K, the k_{RISC} rate can completely compete with the radiative and non-radiative decay rates, thus leading to an occurrence of strong delayed fluorescence.

4 Conclusions

The DFT/TD-DFT methods have been used to explore the geometric and electronic properties of a carbazole-based thermally activated delayed fluorescence molecule. The TVCF rate formalism has been employed to quantitatively estimate the interconversion and deactivation rates of the S_1 and T_1 states at different temperatures. The prompt fluorescence and delayed fluorescence efficiencies, and the total fluorescence efficiency have been obtained correspondingly. The main conclusions are as follows:

(1) The hybrid approach of M06-HF for nuclear and B3LYP for electronic properties is suitable for the D–A-type TADF-active molecule.

(2) With an increase of temperature from 77 to 300 K, the reverse intersystem crossing rate is dramatically increased, whereas there are no obvious changes for the radiative and non-radiative decay rates. At 300 K, the RISC rate can completely compete with the radiative and non-radiative rates.

(3) The prompt fluorescence efficiency, delayed fluorescence efficiency, and the total fluorescence efficiency are evaluated to be 15.8%, 38.7%, and 54.5%, which agree well with the available experimental data (29.4%, 27.3%, and 56.7%).

(4) The free rotation of the carbazole group accounts for the energy conversion between S_1 and T_1. The torsional motions between the D and A units in low frequency regions and the stretching vibrations of the bonds in high frequency regions are responsible for the non-radiative decay from S_1 to S_0.

In summary, the present calculated results not only explain reasonably the experimental phenomena, but also provide a quantitative estimate of the fluorescence efficiency, which would be beneficial for designing and developing novel efficient TADF-based OLED materials.

Conflicts of interest

There are no conflicts to declare.

Acknowledgements

This work was supported by the National Natural Science Foundation of China (NSFC) (Grant No. 21503069 and 21676071). We thank the State Key Laboratory of Physical Chemistry of Solid Surfaces (Xiamen University) and the National Supercomputing Center in Shenzhen (Shenzhen Cloud Computing Center) for providing computational resource and software.

References

1 C. W. Tang and S. A. Vanslyke, *Appl. Phys. Lett.*, 1987, **51**, 913–915.
2 S. R. Forrest, *Nature*, 2004, **428**, 911–918.
3 S. Reineke, F. Lindner, G. Schwartz, N. Seidler, K. Walzer, B. Lüssem and K. Leo, *Nature*, 2009, **459**, 234–238.
4 H. Uoyama, K. Goushi, K. Shizu, H. Nomura and C. Adachi, *Nature*, 2012, **492**, 234–238.
5 S. Reineke, M. Thomschke, B. Lüssem and K. Leo, *Rev. Mod. Phys.*, 2013, **85**, 1245–1293.
6 H. Sasabe and J. Kido, *J. Mater. Chem. C*, 2013, **1**, 1699–1707.
7 Q. Zhang, J. Li, K. Shizu, S. Huang, S. Hirata, H. Miyazaki and C. Adachi, *J. Am. Chem. Soc.*, 2012, **134**, 14706–14709.
8 H. Tanaka, K. Shizu, H. Miyazaki and C. Adachi, *Chem. Commun.*, 2012, **48**, 11392–11394.
9 F. B. Dias, K. N. Bourdakos, V. Jankus, K. C. Moss, K. T. Kamtekar, V. Bhalla, J. Santos, M. R. Bryce and A. P. Monkman, *Adv. Mater.*, 2013, **25**, 3707–3714.
10 J. Lee, K. Shizu, H. Tanaka, H. Nomura, T. Yasuda and C. Adachi, *J. Mater. Chem. C*, 2013, **1**, 4599–4604.
11 K. Masui, H. Nakanotani and C. Adachi, *Org. Electron.*, 2013, **14**, 2721–2726.
12 K. Nasu, T. Nakagawa, H. Nomura, C. J. Lin, C. H. Cheng, M. R. Tseng, T. Yasuda and C. Adachi, *Chem. Commun.*, 2013, **49**, 10385–10387.
13 T. Serevičius, T. Nakagawa, M. C. Kuo, S. H. Cheng, K. T. Wong, C. H. Chang, R. C. Kwong, S. Xia and C. Adachi, *Phys. Chem. Chem. Phys.*, 2013, **15**, 15850–15855.
14 Y. Im and J. Y. Lee, *Chem. Mater.*, 2014, **26**, 1413–1419.

15 D. Zhang, L. Duan, Y. Li, D. Zhang and Y. Qiu, *J. Mater. Chem. C*, 2014, **2**, 8191–8197.
16 Q. Zhang, B. Li, S. Huang, H. Nomura, H. Tanaka and C. Adachi, *Nat. Photonics*, 2014, **8**, 326–332.
17 X. Xiong, F. Song, J. Wang, Y. Zhang, Y. Xue, L. Sun, N. Jiang, P. Gao, L. Tian and X. Peng, *J. Am. Chem. Soc.*, 2014, **136**, 9590–9597.
18 S. Wu, M. Aonuma, Q. Zhang, S. Huang, T. Nakagawa, K. Kuwabara and C. Adachi, *J. Mater. Chem. C*, 2014, **2**, 421–424.
19 C. Mayr, S. Y. Lee, T. D. Schmidt, T. Yasuda, C. Adachi and W. Brütting, *Adv. Funct. Mater.*, 2014, **24**, 5232–5239.
20 K. Kawasumi, T. Wu, T. Zhu, H. S. Chae, T. V. Voorhis, M. A. Baldo and T. M. Swager, *J. Am. Chem. Soc.*, 2015, **137**, 11908–11911.
21 J. W. Sun, J. Y. Baek, K. H. Kim, C. K. Moon, J. H. Lee, S. K. Kwon, Y. H. Kim and J. J. Kim, *Chem. Mater.*, 2015, **27**, 6675–6681.
22 K. Albrecht, K. Matsuoka, K. Fujita and K. Yamamoto, *Angew. Chem., Int. Ed.*, 2015, **54**, 5677–5682.
23 D. R. Lee, B. S. Kim, C. W. Lee, Y. Im, K. S. Yook, S. H. Hwang and J. Y. Lee, *ACS Appl. Mater. Interfaces*, 2015, **7**, 9625–9629.
24 Y. J. Shiu, Y. C. Cheng, W. L. Tsai, C. C. Wu, C. T. Chao, C. W. Lu, Y. Chi, Y. T. Chen, S. H. Liu and P. T. Chou, *Angew. Chem., Int. Ed.*, 2016, **55**, 3017–3021.
25 S. Y. Lee, C. Adachi and T. Yasuda, *Adv. Mater.*, 2016, **28**, 4626–4631.
26 P. Rajamalli, N. Senthilkumar, P. Gandeepan, C. C. Ren-Wu, H. W. Lin and C. H. Cheng, *ACS Appl. Mater. Interfaces*, 2016, **8**, 27026–27034.
27 Y. Xiang, S. Gong, Y. Zhao, X. Yin, J. Luo, K. Wu, Z. H. Lu and C. Yang, *J. Mater. Chem. C*, 2016, **4**, 9998–10004.
28 T. A. Lin, T. Chatterjee, W. L. Tsai, W. K. Lee, M. J. Wu, M. Jiao, K. C. Pan, C. L. Yi, C. L. Chung, K. T. Wong and C. C. Wu, *Adv. Mater.*, 2016, **28**, 6976–6983.
29 K. C. Pan, S. W. Li, Y. Y. Ho, Y. J. Shiu, W. L. Tsai, M. Jiao, W. K. Lee, C. C. Wu, C. L. Chung, T. Chatterjee, Y. S. Li, K. T. Wong, H. C. Hu, C. C. Chen and M. T. Lee, *Adv. Funct. Mater.*, 2016, **26**, 7560–7571.
30 J. W. Sun, J. Y. Baek, K. H. Kim, J. S. Huh, Y. H. Kim and J. J. Kim, *J. Mater. Chem. C*, 2017, **5**, 1027–1032.
31 P. L. dos Santos, J. S. Ward, A. S. Batsanov, M. R. Bryce and A. P. Monkman, *J. Phys. Chem. C*, 2017, **121**, 16462–16469.
32 H. Sasabe, Y. Hayasaka, R. Komatsu, K. Nakao and J. Kido, *Chem. – Eur. J.*, 2017, **23**, 114–119.
33 Y. J. Shiu, Y. T. Chen, W. K. Lee, C. C. Wu, T. C. Lin, S. H. Liu, P. T. Chou, C. W. Lu, I. C. Cheng, Y. J. Lien and Y. Chi, *J. Mater. Chem. C*, 2017, **5**, 1452–1462.
34 Z. Yang, Z. Mao, Z. Xie, Y. Zhang, S. Liu, J. Zhao, J. Xu, Z. Chi and M. P. Aldred, *Chem. Soc. Rev.*, 2017, **46**, 915–1016.
35 R. Komatsu, T. Ohsawa, H. Sasabe, K. Nakao, Y. Hayasaka and J. Kido, *ACS Appl. Mater. Interfaces*, 2017, **9**, 4742–4749.
36 P. Rajamalli, N. Senthilkumar, P. Y. Huang, C. C. Ren-Wu, H. W. Lin and C. H. Cheng, *J. Am. Chem. Soc.*, 2017, **139**, 10948–10951.
37 P. Ganesan, R. Ranganathan, Y. Chi, X. K. Liu, C. S. Lee, S. H. Liu, G. H. Lee, T. C. Lin, Y. T. Chen and P. T. Chou, *Chem. – Eur. J.*, 2017, **23**, 2858–2866.
38 T. T. Bui, F. Goubard, M. Ibrahim-Ouali, D. Gigmes and F. Dumur, *Beilstein J. Org. Chem.*, 2018, **14**, 282–308.
39 C. Y. Chan, L. S. Cui, J. U. Kim, H. Nakanotani and C. Adachi, *Adv. Funct. Mater.*, 2018, **28**, 1706023.
40 Y. Liu, C. Li, Z. Ren, S. Yan and M. R. Bryce, *Nat. Rev. Mater.*, 2018, **3**, 18020.
41 K. Shizu, H. Tanaka, M. Uejima, T. Sato, K. Tanaka, H. Kaji and C. Adachi, *J. Phys. Chem. C*, 2015, **119**, 1291–1297.
42 K. Wang, W. Liu, C. J. Zheng, Y. Z. Shi, K. Liang, M. Zhang, X.-M. Ou and X. H. Zhang, *J. Mater. Chem. C*, 2017, **5**, 4797–4803.
43 H. Sun, C. Zhong and J. L. Brédas, *J. Chem. Theory Comput.*, 2015, **11**, 3851–3858.
44 J. Fan, L. Cai, L. Lin and C. Wang, *Chem. Phys. Lett.*, 2016, **664**, 33–38.
45 K. Liang, C. Zheng, K. Wang, W. Liu, Z. Guo, Y. Li and X. Zhang, *Phys. Chem. Chem. Phys.*, 2016, **18**, 26623–26629.
46 J. Zhang, H. Yuan, S. Feng, K. Wen and X. Guo, *Spectrochim. Acta, Part A*, 2018, **202**, 102–106.
47 Q. Peng, D. Fan, R. H. Duan, Y. Yi, Y. Niu, D. Wang and Z. Shuai, *J. Phys. Chem. C*, 2017, **121**, 13448–13456.
48 J. Fan, Y. Zhang, Y. Zhou, L. Lin and C. K. Wang, *J. Phys. Chem. C*, 2018, **122**, 2358–2366.
49 Q. Peng, Y. Niu, Q. Shi, X. Gao and Z. Shuai, *J. Chem. Theory Comput.*, 2013, **9**, 1132–1143.
50 Y. Tao, K. Yuan, T. Chen, P. Xu, H. Li, R. Chen, C. Zheng, L. Zhang and W. Huang, *Adv. Mater.*, 2014, **26**, 7931–7958.
51 Q. Peng, Y. Yi, Z. Shuai and J. Shao, *J. Chem. Phys.*, 2007, **126**, 114302.
52 Y. Niu, Q. Peng, C. Deng, X. Gao and Z. Shuai, *J. Phys. Chem. A*, 2010, **114**, 7817–7831.
53 M. J. Frisch, G. W. Trucks, H. B. Schlegel, G. E. Scuseria, M. A. Robb, J. R. Cheeseman, G. Scalmani, V. Barone, B. Mennucci, G. A. Petersson, H. Nakatsuji, M. Caricato, X. Li, H. P. Hratchian, A. F. Izmaylov, J. Bloino, G. Zheng, J. L. Sonnenberg, M. Hada, M. Ehara, K. Toyota, R. Fukuda, J. Hasegawa, M. Tshida, T. Nakajima, Y. Honda, O. Kitao, H. Nakai, T. Vreven, J. A. Montgomery, J. E. Peralta, F. Ogliaro, M. Bearpark, J. J. Heyd, E. Brothers, K. N. Kudin, V. N. Staroverov, R. Kobayashi, J. Normand, K. Raghavachari, A. Rendell, J. C. Burant, S. S. Tyengar, J. Tomasi, M. Cossi, N. Rega, J. M. Millam, M. Klene, J. E. Knox, J. B. Cross, V. Bakken, C. Adamo, C. Jaramillo, J. W. Ochterski, R. L. Martin, K. Morokuma, V. G. Zakrzewski, G. A. Voth, P. Salvador, J. J. Dannenberg, S. Dapprich, A. D. Daniels, Ö. Farkas, J. B. Foresman, J. V. Ortiz, J. Cioslowski and D. J. Fox, *Gaussian 09, Revision A.02*, Gaussian, Inc., Wallingford, CT, 2009.
54 Q. Peng, Y. Yi, Z. Shuai and J. Shao, *J. Am. Chem. Soc.*, 2007, **129**, 9333–9339.
55 Y. Niu, W. Li, Q. Peng, H. Geng, Y. Yi, L. Wang, G. Nan, D. Wang and Z. Shuai, *Mol. Phys.*, 2018, **116**, 1078–1090.
56 O. Vahtras, H. Ågren, P. Jørgensen, H. J. A. Jensen, T. Helgaker and J. Olsen, *J. Chem. Phys.*, 1992, **97**, 9178–9187.

57 K. Aidas, C. Angeli, K. L. Bak, V. Bakken, R. Bast, L. Boman, O. Christiansen, R. Cimiraglia, S. Coriani, P. Dahle, E. K. Dalskov, U. Ekström, T. Enevoldsen, J. J. Eriksen, P. Ettenhuber, B. Fernández, L. Ferrighi, H. Fliegl, L. Frediani, K. Hald, A. Halkier, C. Hättig, H. Heiberg, T. Helgaker, A. C. Hennum, H. Hettema, E. Hjertenaes, S. Høst, I. M. Høyvik, M. F. Iozzi, B. Jansík, H. J. Jensen, D. Jonsson, P. Jørgensen, J. Kauczor, S. Kirpekar, T. Kjaergaard, W. Klopper, S. Knecht, R. Kobayashi, H. Koch, J. Kongsted, A. Krapp, K. Kristensen, A. Ligabue, O. B. Lutnaes, J. I. Melo, K. V. Mikkelsen, R. H. Myhre, C. Neiss, C. B. Nielsen, P. Norman, J. Olsen, J. M. Olsen, A. Osted, M. J. Packer, F. Pawlowski, T. B. Pedersen, P. F. Provasi, S. Reine, Z. Rinkevicius, T. A. Ruden, K. Ruud, V. V. Rybkin, P. Salek, C. C. Samson, A. S. de Merás, T. Saue, S. P. Sauer, B. Schimmelpfennig, K. Sneskov, A. H. Steindal, K. O. Sylvester-Hvid, P. R. Taylor, A. M. Teale, E. I. Tellgren, D. P. Tew, A. J. Thorvaldsen, L. Thøgersen, O. Vahtras, M. A. Watson, D. J. Wilson, M. Ziolkowski and H. Ågren, *WIREs Comput. Mol. Sci.*, 2014, **4**, 269–284.
58 S. Feng, K. Wen, Y. Si, X. Guo and J. Zhang, *J. Comput. Chem.*, 2018, **39**, 2601–2606.
59 Z. Shuai and Q. Peng, *Phys. Rep.*, 2014, **537**, 123–156.
60 T. Lu and F. Chen, *J. Comput. Chem.*, 2012, **33**, 580–592.
61 A. Simperler, A. Kornherr, R. Chopra, P. A. Bonnet, W. Jones, W. D. S. Motherwell and G. Zifferer, *J. Phys. Chem. B*, 2006, **110**, 19678–19684.
62 *Materials Studio 7.0*, Accelrys Software, Inc., San Diego, CA, 2013.
63 H. Sun, *J. Phys. Chem. B*, 1998, **102**, 7338–7364.
64 M. J. Hwang, T. P. Stockfisch and A. T. Hagler, *J. Am. Chem. Soc.*, 1994, **116**, 2515–2525.
65 S. W. Bunte and H. Sun, *J. Phys. Chem. B*, 2000, **104**, 2477–2489.